Coaxial volumetric velocimetry

Schneiders, Jan F.G.; Scarano, Fulvio; Jux, Constantin; Sciacchitano, Andrea

DOI
10.1088/1361-6501/aab07d

Publication date
2018

Document Version
Final published version

Published in
Measurement Science and Technology

Citation (APA)
Schneiders, J. F. G., Scarano, F., Jux, C., & Sciacchitano, A. (2018). Coaxial volumetric velocimetry. *Measurement Science and Technology*, *29*(6), Article 065201. https://doi.org/10.1088/1361-6501/aab07d

PAPER

Coaxial volumetric velocimetry

To cite this article: Jan F G Schneiders *et al* 2018 *Meas. Sci. Technol.* **29** 065201

IOP Publishing Measurement Science and Technology
Meas. Sci. Technol. **29** (2018) 065201 (15pp) https://doi.org/10.1088/1361-6501/aab07d

Coaxial volumetric velocimetry

Jan F G Schneiders, Fulvio Scarano, Constantin Jux and Andrea Sciacchitano

Department of Aerospace Engineering, TU Delft, Delft, Netherlands

E-mail: j.f.g.schneiders@tudelft.nl

Received 25 October 2017, revised 24 January 2018
Accepted for publication 19 February 2018
Published 17 April 2018

Abstract

This study describes the working principles of the coaxial volumetric velocimeter (CVV) for wind tunnel measurements. The measurement system is derived from the concept of tomographic PIV in combination with recent developments of Lagrangian particle tracking. The main characteristic of the CVV is its small tomographic aperture and the coaxial arrangement between the illumination and imaging directions. The system consists of a multi-camera arrangement subtending only few degrees solid angle and a long focal depth. Contrary to established PIV practice, laser illumination is provided along the same direction as that of the camera views, reducing the optical access requirements to a single viewing direction. The laser light is expanded to illuminate the full field of view of the cameras. Such illumination and imaging conditions along a deep measurement volume dictate the use of tracer particles with a large scattering area. In the present work, helium-filled soap bubbles are used. The fundamental principles of the CVV in terms of dynamic velocity and spatial range are discussed. Maximum particle image density is shown to limit tracer particle seeding concentration and instantaneous spatial resolution. Time-averaged flow fields can be obtained at high spatial resolution by ensemble averaging. The use of the CVV for time-averaged measurements is demonstrated in two wind tunnel experiments. After comparing the CVV measurements with the potential flow in front of a sphere, the near-surface flow around a complex wind tunnel model of a cyclist is measured. The measurements yield the volumetric time-averaged velocity and vorticity field. The measurements of the streamlines in proximity of the surface give an indication of the skin-friction lines pattern, which is of use in the interpretation of the surface flow topology.

Keywords: PIV, tomographic PIV, HFSB, particle tracking, CVV, volumetric measurement, optical access

(Some figures may appear in colour only in the online journal)

1. Introduction

Just over a decade since its introduction, tomographic PIV (Elsinga *et al* 2006) has become the benchmark technique for volumetric wind tunnel measurements. The technique employs a measurement setup similar to planar PIV and uses a laser to illuminate a relatively thin measurement volume. The tomographic imaging system features multiple cameras that subtend a finite solid angle, where accuracy of the particle field reconstruction is maximized for a total aperture ranging between 40 and 80° (Elsinga *et al* 2006, Scarano 2013). The axis of the tomographic imaging system (z-axis in figure 1) is often approximately perpendicular to the illumination direction (x-axis in figure 1). A typical tomographic PIV system is illustrated in figure 1. The tomographic PIV setup relies upon the available optical access, a stable structure to support the multiple cameras and extensive pre- and post-calibration to achieve an accurate mapping function between the object space and the images. The distance between the cameras is typically significantly larger than the camera size, as a direct consequence of requirements for the system angular aperture to range typically between 40 and 80°. Therefore, the availability of small cameras does not allow a compacting the measurement system. This limits the versatile application of tomographic PIV, in particular when complex shapes (i.e. non-convex shapes or multiple objects) are investigated for instance during wind tunnel experiments.

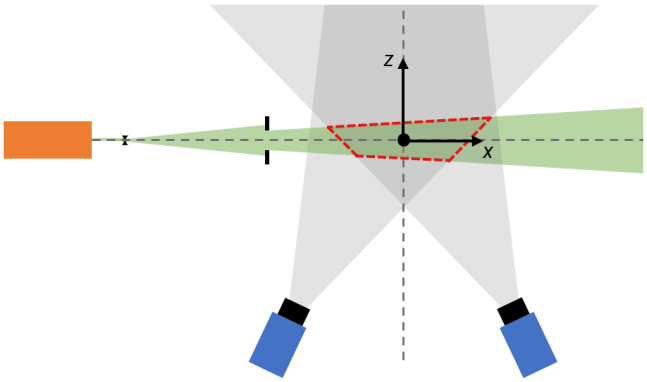

Figure 1. Measurement setup for tomographic PIV, showing the cameras (blue), field of view (grey) and laser illumination (green). Measurement volume contoured by the dashed red line.

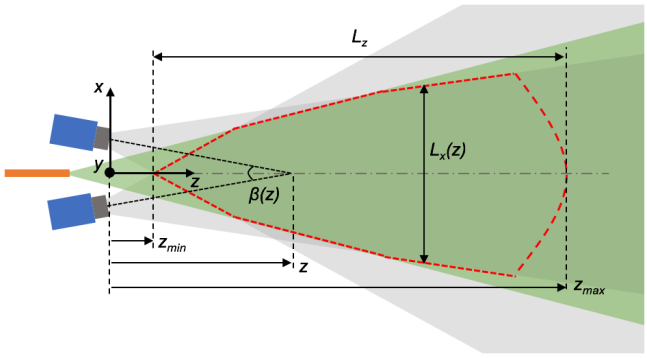

Figure 2. Measurement setup for a coaxial velocimeter (CVV), showing the cameras (blue), field of view (grey) and laser illumination (green) provided from an optical fiber (orange).

Near wall measurements and the evaluation of the near-surface flow topology by planar and tomographic PIV has remained largely limited to straight surfaces or concave with curvature along a single direction (e.g. airfoils). A relevant example is given by Depardon *et al* (2005), who performed a series of near-wall PIV measurements aligned with the straight faces of a square cylinder. This yielded the arrangement of time-averaged skin-friction lines. When dealing with fully 3D curved surfaces, however, the application of PIV is limited by the optical access requirements, or requires a facility and model that permit refractive index matching (e.g. Talapatra and Katz (2012) and Johnson *et al* (2017)).

Multiple efforts have been devoted in other directions to reduce system size and optical access requirements. In-line holographic PIV (Meng *et al* 2004, amongst others) achieves a measurement system where the imaging and illumination systems are positioned along one axis, where typically laser illumination is used from the opposite side of the camera. With the same technique, the 3D velocity field over complex rough walls was inspected in a facility that permits refractive index matching (Talapatra and Katz 2012).

In addition, systems that reduce the requirement for imaging optical access have made use of the plenoptic concept (Fahringer *et al* 2015), astigmatic aberrations (Hain and Kähler 2006) or defocusing (Willert and Gharib 1992). Mainly for application in liquid flows, volumetric velocimetry using a compact three-sensor system was recently achieved by the V3V system (Pothos *et al* 2009). This system obtains particle depth measurements from the size of particle triangle patterns resulting from superposition of three camera images, following the defocusing concept (Willert and Gharib 1992). Despite the variety of working principles, the above systems are typically operated with illumination and imaging along approximately perpendicular directions.

A coaxial measurement configuration would bring imaging and illumination along the same direction. Such a configuration can be realized by introducing two main modifications to the tomographic PIV measurement setup: (1) reduction of the tomographic aperture β by an order of magnitude; (2) coaxial arrangement between the illumination and imaging directions. As a result, the imaging system comprises a number of compact cameras that are positioned at small relative distance (figure 2). The laser light, transmitted by an optical fiber, is emitted from the probe in between the cameras and expanded along a cone to match their field of view at a prescribed distance. The resulting coaxial volumetric velocimeter (CVV) can be integrated in a single module in a way similar to that of laser Doppler anemometry operating in back-scatter mode (Durst *et al* 1976).

A first stumbling block of the coaxial setup is related to particle image detectability. While typical volumetric experiments feature a negligible variation in object distance compared to the overall operating distance, such variation is significant for the CVV measurement domain. The deep illuminated volume realized by the coaxial system (dashed red line figure 2) requires a small imaging aperture for particles to be imaged in-focus, which reduces the overall amount of light collected on the imager. In addition, the laser light intensity remains relatively uniform and focused for planar or tomographic PIV to achieve sufficient light scattering from micron sized tracer particles. Instead, in the coaxial configuration the laser light is expanded from its source point to illuminate the full camera field of view. The combination of the above effects produces adverse conditions in terms of particle image intensity variability, which need to be accounted for while designing the CVV system. The problem is addressed in the present study by introduction of tracers with a high scattering efficiency. The scattered light from helium filled soap bubbles as flow tracers (HFSB, Bosbach *et al* 2009) has been reported to be 10^4–10^5 times more intense (for a bubble diameter in the sub-millimeter range) than that of micrometer droplets (Caridi and Sciacchitano 2017) enabling a significant increase of the measurement domain for tomographic PIV experiments. The suitability of helium-filled soap bubbles for wind tunnel measurements at relatively large scale was recently ascertained in a series of studies (Scarano *et al* 2015, Caridi *et al* 2016, Schneiders *et al* 2016).

A second stumbling block stems from the very small tomographic aperture of the imaging system of the CVV. This leads to a poor positional accuracy of particle tracers along the depth direction (Elsinga *et al* 2006, Fahringer *et al* 2015; amongst others). The problem is dealt with by a substantial increase of the time interval along which the particle motion is followed. Registration of the particle position over multiple frames

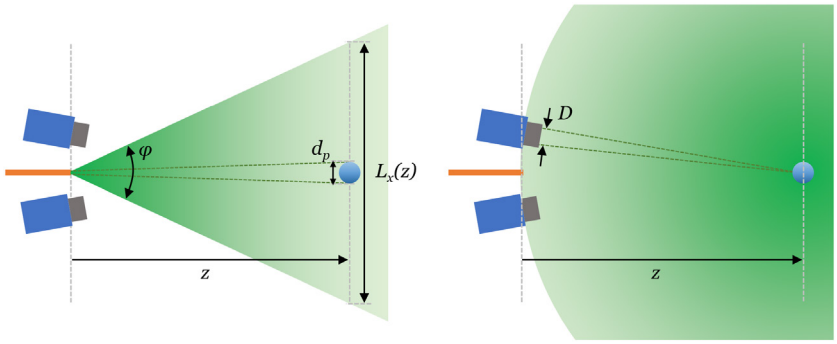

Figure 3. Schematic illustration of laser light propagated from the optical fiber, interacting with a tracer particle (left) and collected back by the cameras (right). Arrangement of optical fiber (orange) in between the cameras (blue) for illustration purposes. Tracer particle not drawn to scale.

yields a longer trajectory and in turn increases the velocity dynamic range compared to double-pulse systems (Shake-the-Box, Schanz *et al* 2016, amongst others). Therefore, the time-resolved measurement condition needed for CVV requires the use of high-speed CMOS cameras and diode-pumped solid-state lasers operating in the kilohertz range.

The work discusses first the fundamental properties of the CVV in terms of hardware configuration, illumination and imaging optics, followed by the data analysis procedure. The system performance is estimated in terms of measurement accuracy and spatial resolution of the time-averaged velocity field. Finally, wind tunnel experiments illustrate the typical data output and the potential of the CVV for the investigation of aerodynamic flows.

2. Measurement range and resolvable flow scales

2.1. Measurement volume

Tomographic PIV is taken here as a term of comparison when evaluating the spatial dynamic range of the CVV technique. In tomographic PIV, the depth of the measurement volume is often controlled by cutting of the laser beam with knife edge filters. The measurement volume of the CVV (dashed red line in figure 2) results from the propagation of the laser beam expanding conically with a given angle φ. The cameras angle of view is chosen to approximately coincide with φ.

2.1.1. Measurement volume width and height. Assuming that the illumination covers the full field of view, both the width L_x and height L_y of the measurement volume are dependent on the sensor size ($W \times H$) and optical magnification M

$$L_x(z) = \frac{W}{M}, \tag{1}$$

and similarly, $L_y(z) = H/M$. In the imaging regime of CVV, the magnification cannot be considered constant as it varies widely within the measurement domain. The magnification is inversely proportional to the distance z from the imaging system:

$$M = \frac{d_i}{z} \approx \frac{f}{z}, \tag{2}$$

where d_i is the distance of the lens from the image plane. The former can be approximated by the focal length, f, of the lens when $M \ll 1$.

2.1.2. Measurement volume depth. The depth of the measurement volume is limited by the laser pulse energy, and the camera sensitivity and its noise level. The laser light expands at an angle φ (figure 3) after a single spherical lens from the exit of the fiber optic laser guide. Given the conical propagation of illumination, the laser light intensity decays with the square of the distance z. The angle φ needs to be sufficiently large for the illumination to cover the field of view and can be approximated by

$$\varphi \geqslant 2a \tan \frac{L_x}{2z}. \tag{3}$$

A particle of diameter d_p placed at distance z will scatter the light back towards the imagers collecting it through an aperture D. Considering the spherical propagation by an angle φ of a laser light pulse of energy I_0 from the fiber end (fiber diameter d_f), the expression of the collected light I_p reads as

$$I_\mathrm{p} = I_0 \frac{d_\mathrm{f}^2}{z^2 \tan^2\left(\frac{1}{2}\varphi\right)} \frac{Q\pi d_\mathrm{p}^2 D^2}{z^2} \tag{4}$$

where Q is the optical scattering efficiency of the soap bubble in backward direction (figure 3), defined as the ratio between the amount of light received by the bubble and the amount of light scattered back in the direction of the CVV. In the above equation, the first ratio on the right hand side term describes the light extinction due to propagation from the source to the tracer. The second ratio models the amount of light that is scattered and subsequently collected on the camera sensor, where it can be seen that more light is collected when the aperture D is increased.

An important conclusion is that the particle image intensity I_p decreases moving away along the measurement volume depth with the power four:

$$I_\mathrm{p} \propto \frac{1}{z^4}. \tag{5}$$

The above scaling is experimentally verified by imaging particles placed within a range of distances. The experiment is performed with the CVV system realized in section 6. The

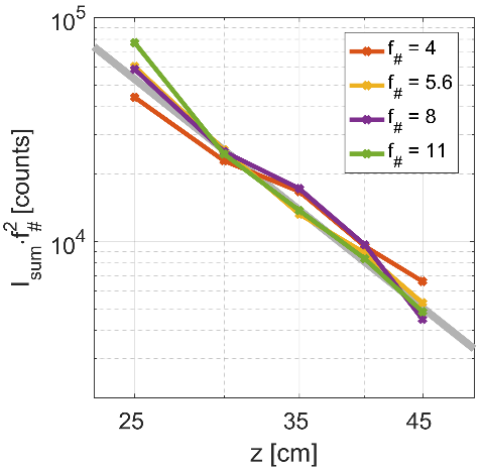

Figure 4. Particle image integral intensity measured by the CVV system. The grey line indicates the theoretical slope of −4 on the log–log scale.

position of the tracers is controlled by translating a single HFSB generator along the depth of the measurement volume. The intensity of tracers right at the exit of the HFSB generator is evaluated. In figure 4 the integral of particle image intensity is shown. The numerical aperture $f_\#$ is varied from 4 to 11. The results expressed in logarithmic scale agree with fourth-power scaling (grey line). Also, premultiplying by $f_\#^2$ to account for the different aperture used in the experiments makes the data series collapse consistently with equation (4).

Given this fourth order relationship between particle image intensity and z, one can relate the achievable depth of measurement to the imager bit depth. The ratio between the volume depth, or maximum measurement distance, z_{max} and the closest position where particle images begin to produce intensity saturation z_{sat} equals

$$\frac{z_{max}}{z_{sat}} = \left(\frac{2^b}{I_n}\right)^{\frac{1}{4}}, \tag{6}$$

where I_n is the minimum detectable particle image intensity and b the imager bit depth. The exponent is due to the fourth order relation between particle image intensity and distance. For illustration, a 10-bit camera with a minimum level for detectability of 20 counts allows for $z_{max} \approx 50$ cm. In these conditions, particles closer than 20 cm are imaged at saturated intensity.

2.1.3. Measurement volume size. Using the expression for the measurement volume width (equation (1)), the measurement volume of the CVV can be approximated by a truncated square pyramid with a height corresponding to the difference between maximum and minimum distance along depth. The CVV system hereafter (section 6) features an angle of view of approximately $\varphi = 50°$. Considering a closest measurement distance of $z_{min} = 10$ cm and a furthest $z_{max} = 50$ cm, the resulting measurement volume is approximately 30 liters. Here z_{min} is taken smaller than z_{sat} as particles with saturated intensity can still be easily detected and tracked. It should be remarked, however, that the aerodynamic interference of the CVV device with the fluid stream becomes non-negligible at such short distance from it. A detailed discussion is given in Jux *et al* (2018). Moreover, given the compactness and fixed camera configuration of the CVV, the device is intended to be pointed in several directions and translated with the aid of a robotic arm (Jux *et al* 2018).

2.2. Spatial resolution

The estimation of the time-averaged velocity vector field is obtained by ensemble averaging the value of the instantaneous velocity obtained for each particle trajectory within an interrogation bins or cells. Ample discussion of possible data processing techniques is given in Kähler *et al* (2012a, 2012b). Furthermore, optimized rules for ensemble averaging have been recently proposed by Agüera *et al* (2016). For sake of simplicity, the averaging procedure consists of an ensemble average of all velocity samples from particle trajectories that intersect with the interrogation bin.

The number of discrete particle velocity measurements N_I within a cubic element or bin with a volume l_B^3 depends upon the instantaneous concentration of the tracers, C, and the number of measurement time-instants, N_t, that is considered for ensemble averaging:

$$N_I = l_B^3 C N_t \;\Rightarrow\; l_B = \sqrt[3]{\frac{N_I}{N_t C}}, \tag{7}$$

which can accordingly be rewritten to obtain an expression for the linear size of the bin, l_B. Producing a statistically converged estimate of the average velocity within a cubic element or bin requires that a sufficient number of uncorrelated velocity measurements are captured within a bin. This can be achieved by (i) increasing the bin size, (ii) increasing seeding concentration, or (iii) increasing the amount of recordings collected within an experiment. In practice, a particle appears typically only once in a bin and therefore for simplicity the number of uncorrelated measurement time-instants is assumed equal to the total number of measurement time-instants.

The upper limit for the tracer particle seeding concentration C_{max} is dictated by the maximum particle image density often expressed as N_p in particles per pixel (ppp). Considering the latter:

$$N_p = C\frac{V}{N_{pix}} \;\Rightarrow\; C_{max} = N_{p,max}\frac{N_{pix}}{V}, \tag{8}$$

where N_{pix} is the number of pixels of the imager and V is the measurement volume size. Tomographic reconstruction is reliably obtained up to $N_p = 0.05$ ppp (Elsinga *et al* 2006, among others). A similar value has been demonstrated for the STB algorithm (Schanz *et al* 2016) and this value is retained as upper bound for the CVV. This value dictates the maximum tracer particle concentration according to equation (8). Considering $z_{min} = 10$ cm and $z_{max} = 50$ cm, equation (8) yields a maximum concentration of approximately 1 particle cm^{-3}.

Because seeding concentration cannot be arbitrarily increased and is limited to a relatively low number on the

order of 1 particle cm^{-3} in practical situations, the bin size l_B typically cannot be reduced by increasing the seeding concentration. Instead, a small bin size and consequently high spatial resolution can be obtained with the CVV only by increasing the number of recordings N_t leading to a longer the acquisition time.

3. Particle imaging and velocity estimation

3.1. Lens aperture and focus

The measurement volume of the CVV requires a significantly larger depth of field (DOF) than a typical tomographic PIV apparatus. To avoid that particles are imaged out-of-focus, the near and far limits of the DOF, D_N and D_F, should include the range between z_{min} and z_{max} respectively (figure 2). The limits D_N and D_F can be approximated by Larmore (1965):

$$z_{min} \geqslant D_N = \frac{Hz_f}{H + z_f} \tag{9}$$

$$z_{max} \leqslant D_F = \frac{Hz_f}{H - z_f}, \quad \text{for } z_f < H, \tag{10}$$

where z_f is the focal plane and H is the hyperfocal distance. The latter, for the CVV, is equal to

$$H = \frac{f^2}{f_\# d_\tau}, \tag{11}$$

where $f_\#$ is the numerical aperture of the objective, and where similar to Raffel *et al* (2007) the circle of confusion was set equal to the particle image size d_τ (equation (14)). Solving the above equations for the minimum $f_\#$ yields

$$z_f = \frac{2z_{min}z_{max}}{z_{min} + z_{max}} \tag{12}$$

$$f_{\#,min} = \frac{1}{2}\frac{f^2}{d_\tau}\left(\frac{1}{z_{min}} - \frac{1}{z_{max}}\right). \tag{13}$$

Therefore the focal plane of the CVV should not be centered, but be closer to D_N than to D_F. The CVV realized in section 6, for instance, is focused at $z_f = 17$ cm, when $z_{min} = 10$ cm and $z_{max} = 50$ cm. The minimum aperture setting to ensure the full measurement volume in focus requires is $f_\# = 7$. A higher aperture setting of 8 is desired, however, to achieve particle images larger than 2 pixels (section 3.2).

3.2. Particle image size and displacement

Considering that the optical magnification of CVV varies between 10^{-1} and 10^{-2} the particle image size is dominated by diffraction with a rather constant value along the entire measurement volume depth. In backward scattering mode, the distance between glare points of the HFSB vanishes below the diffraction limit. Therefore, the particle image size is well approximated by diffraction only and reads as

$$d_\tau = 2.44\lambda f_\# (1 + M). \tag{14}$$

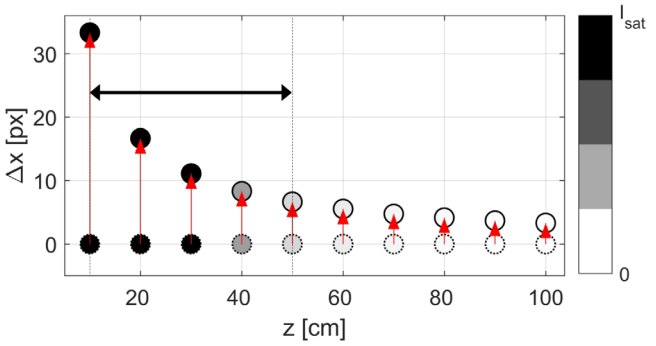

Figure 5. Particle image displacement along the measurement volume depth in case of a constant free-stream particle displacement of 4 mm. The color indicates the particle intensity. The typical working range of a CVV is indicated by the black arrow.

The particle image displacement is inversely proportional to distance according to

$$\Delta x_i = Mu\Delta t = u\Delta t\frac{f}{z}, \tag{15}$$

where Δt is the pulse separation time. Therefore, particles close to the camera appear travelling faster than particles further away. This is illustrated in figure 5 in case of the CVV realized in section 6 and a constant free-stream particle displacement of 4 mm. The working range of the CVV (Jux *et al* 2018) is indicated in the figure by the black arrow.

4. Velocity resolution

4.1. Estimation of particle position

Measuring the position of a particle tracer is affected by an uncertainty ϵ_x proportional to the particle image size:

$$\epsilon_x = c_\tau d_\tau, \tag{16}$$

which holds when d_τ is approximately 1.5 times larger than the pixel size (e.g. Raffel *et al* (2007)) and where the coefficient c_τ represents the uncertainty in locating the centroid of the particle image (Adrian 1991, Adrian and Westerweel 2011). This coefficient typically falls in the range 0.1–0.2.

In case of 3D measurements, the relevant property is the reconstructed particle size, whereby the particle image is reprojected to physical space. The reconstructed particle size along the x- and y-axis depends almost entirely upon the particle image size:

$$d_x = d_y = \frac{d_\tau}{M}. \tag{17}$$

Therefore, in case of 3D measurements:

$$\epsilon_x = \frac{c_\tau d_\tau}{M}. \tag{18}$$

Particle reconstruction along z depends upon the system aperture β. In the case of tomographic PIV, the limited solid angle subtended by the camera typically causes the particles to be elongated two to three times (figure 6, Elsinga *et al* 2006, Fahringer *et al* 2015; amongst others).

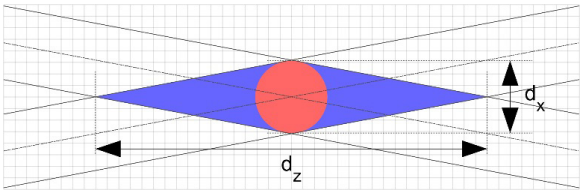

Figure 6. Schematic of the reconstructed particle intensity.

For small aperture ($\beta \ll 1$ rad), the extent of the particle elongation is linearly dependent from β as follows:

$$\frac{d_z}{d_x} = \frac{2}{\beta}. \tag{19}$$

It should be kept in mind that the angle β is not a constant as it decreases by increasing distance z,

$$\beta = \frac{\beta_0 z_0}{z}, \tag{20}$$

with β_0 the local solid angle at chosen position z_0 (see figure 2). For illustration, taking the CVV realized in section 6 at $z = 30$ cm, a local value of $\beta = 7°$ corresponds to a particle elongation of factor 16. If a particle is imaged at a diffraction limited size of 2 pixels the region of high intensity in 3D space will be of the extent of $d_x = d_y = 0.7$ mm and $d_z = 12$ mm.

Consequently, the particle positional uncertainty in the z-direction is significantly larger than in the other two directions:

$$\epsilon_z = \frac{2}{\beta}\epsilon_x. \tag{21}$$

Assuming $c_\tau = 0.1$ for equation (18), an instantaneous particle positional error $\epsilon_x = 0.1$ mm translates into $\epsilon_z = 1$ mm. As discussed in the remainder, this effect needs to be compensated by enlarging the particle displacement ΔX:

$$\frac{\Delta X}{\epsilon_z} \gg 1. \tag{22}$$

Extending overly the time separation in two-pulse systems increases the effect of temporal truncation of the tracer velocity estimation (Boillot and Prasad 1996). The latter effect is countered by sampling the particle position at multiple times and analyzing its trajectory by multi-framing techniques, as discussed in detail in the next section.

4.2. Uncertainty of instantaneous velocity vector estimation

For double pulse systems, the relative measurement uncertainty of the particle displacement estimation is approximated from superposition of the variances of the particle position estimation:

$$\epsilon_u = \frac{\epsilon_x\sqrt{2}}{\Delta x} = \frac{\epsilon_x\sqrt{2}}{u\Delta t}, \tag{23}$$

where Δx is the particle displacement and Δt is the pulse-separation time.

Estimating the velocity from multiple frames allows for a reduction of the velocity measurement error (Cierpka *et al* 2013, Lynch and Scarano 2013, Schanz *et al* 2016; amongst others). The concept of track regularization is illustrated in figure 7, where a second order polynomial (i.e. Savitzky-Golay filter, Savitzky and Golay (1964)) is fitted through discrete particle positions including the effect of the non-isotropic reconstruction. While multi-frame approaches exist for cross-correlation analysis (Lynch and Scarano 2013, Jeon *et al* 2014), the analysis for the CVV is limited to volumetric Lagrangian particle tracking approaches (e.g. Novara *et al* (2013) and Schanz *et al* (2016)).

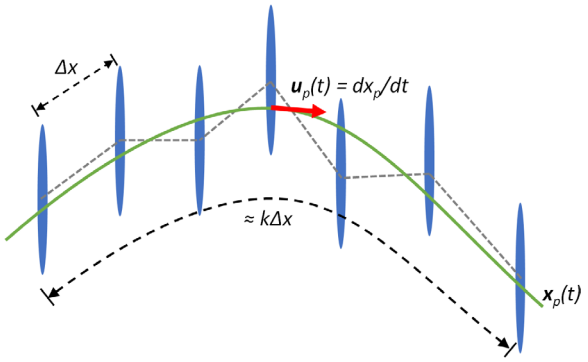

Figure 7. Schematic of a particle trajectory evaluated along a discrete number of exposure and with particle elongation due to the low tomographic aperture. The grey dotted lines show the result from two-frame analysis and green line shows a second order polynomial fit over a track length of $k\Delta x$.

With multi-frame analysis of k frames, two effects contribute to the error reduction: the first is given by the longer overall time separation according to equation (23) by a factor k. Secondly the error reduction with factor $\sqrt{k}$ is obtained when averaging of random error corresponding to the particle position estimation from each sample along the integral path length (figure 7). The combined effects yield a scaling of the error with $k^{-3/2}$ already retrieved for the analysis based on cross-correlation (Lynch and Scarano 2013). The resulting expression for the relative velocity uncertainty when using multi-frame analysis reads as

$$\epsilon_u = \frac{c_\alpha \epsilon_x}{k\Delta x\sqrt{k}}, \tag{24}$$

where c_α is a coefficient dependent upon the particle track regularization technique that is used and Δx is the displacement between two subsequent exposures of the multi-frame recording. The above expression is valid under the hypothesis that the particle trajectory is fitted with a function that avoids truncation of the velocity variations along the trajectory. Typically, polynomials of order 2–3 have been used with multi-frame recordings of length k ranging from 5 to 15 (Novara *et al* 2013, Schanz *et al* 2013, Schneiders *et al* 2016; amongst others). A general description and automatic criterion to select the optimal polynomial order and kernel size that avoids truncation is a topic of ongoing research. The recent work of Schanz *et al* (2016) proposes to use a Wiener filter and Gesemann *et al* (2016) propose to use a B-Spline fitting that yields a similar result as the Wiener filter. For details on optimal track fitting, the reader is referred to these works.

In the following paragraphs, the order of magnitude of the CVV velocity measurement error is approximated based upon a polynomial fit in the assumption that the particle trajectories are not truncated (i.e. low-pass filtered). A polynomial fitting procedure returns an analytical expression for the temporal evolution of the tracer position $\boldsymbol{x}_\mathrm{p}(t)$:

$$\boldsymbol{x}_\mathrm{p}(t) = \boldsymbol{a}_1 + \boldsymbol{a}_2 t + \boldsymbol{a}_3 t^2 \;\rightarrow\; \boldsymbol{u}_\mathrm{p}(0) = \boldsymbol{a}_2. \tag{25}$$

In the above example the Taylor expansion is truncated to the second order. The particle velocity is subsequently obtained from the time derivative of the above expression. For a time-centered estimate, the velocity corresponds to the coefficient $\boldsymbol{a}_2$.

The work of Schneiders and Sciacchitano (2017) establishes that $c_\alpha \approx 3.5$ in equation (24) for a second order polynomial, under the assumption that truncation errors (low-pass filtering) are negligible.

In conclusion, an operational criterion is proposed here for low-aperture systems ($\beta \ll 1$ rad). The criterion dictates the minimum number of exposures k to be included in the trajectory estimation that will return a velocity estimate with the component along depth of accuracy comparable to that of the in-plane components as obtained with a double-pulse system:

$$k \geqslant 3/\beta^{\frac{2}{3}}. \tag{26}$$

Note that when using this criterion, the uncertainty of the in-plane component will also reduce and hence the uncertainty of the velocity component along depth direction always remain higher than that of the in-plane components. Considering, for instance, an aperture $\beta = 0.1$ radians and a sequence of 10 frames, where the particle displacement between frames is 5 mm, the measurement uncertainty for u and v components is approximately 0.2% and approximately 4% for the w component.

4.3. Uncertainty of time-averaged velocity estimation

The discussion in the previous section pertains to the uncertainty of the instantaneous velocity measurements. When dealing with the estimation of time-averaged velocity, the uncertainty is typically dominated by the temporal velocity fluctuations due for instance to flow turbulence. The dependence of time-average estimation uncertainty upon the latter and the number of samples considered for ensemble averaging reads as follows:

$$\epsilon_{\bar{u}} = \frac{\sqrt{\sigma_u^2 + \epsilon_u^2}}{\sqrt{N_\mathrm{I}}} \approx \frac{\sigma_u}{\sqrt{N_\mathrm{I}}}, \tag{27}$$

where σ_u is the turbulence intensity and N_I is the number of velocity measurements in the bin used for ensemble averaging (section 2.2). The second approximate equality holds when $\sigma_u \gg \epsilon_u$.

The uncertainty of the time-averaged velocity vector field therefore largely depends upon the number of velocity measurements in the ensemble averaging bin. A trade-off between measurement accuracy and spatial resolution emerges clearly from the above discussion, since increasing the number of samples N_I implies a larger size of the bin chosen for ensemble averaging.

5. Dynamic spatial and velocity range

Here, the ranges of resolvable velocity field variations and spatial scales are estimated considering the properties of the CVV measurement system. The smallest resolvable length scale in the velocity field stems from the interrogation bin size l_B (section 2.2), whereas the largest resolvable scale is determined by the measurement volume size (section 2.1). Given the compactness of the device, the latter can be expanded by moving the measurement region with the aid of a traversing mechanism or a robotic arm, as demonstrated in Jux *et al* (2018).

Adrian (1997) defined the dynamic spatial range (DSR) as the ratio between the largest and smallest resolvable measurement scales for instantaneous measurements. Analogously, the DSR for time-averaged CVV measurements can be defined using the length scales derived above:

$$\overline{\mathrm{DSR}} = \frac{L_x}{l_\mathrm{B}}, \tag{28}$$

where L_x is selected as a typical dimension of the measurement domain (section 2.1). Assuming a measurement domain extent of 50 cm and a bin size of 1 cm^3, the resulting $\overline{\mathrm{DSR}}$ is in the order of 50. This is above that obtained with large-scale tomographic PIV experiments, where a dynamic spatial range between 20 and 30 is obtained (Caridi *et al* 2016), with the caveat that the latter refers to the instantaneous measurements. So far, tomographic measurements where the time-average velocity was obtained at higher resolution using correlation averaging have not been reported in the literature.

Similar to the above, the dynamic velocity range (DVR, Adrian 1997) can be defined for the time-averaged velocity measurements, as the ratio between the highest value of measured velocity and the smallest resolvable variation. The latter depends upon the velocity measurement uncertainty as derived in section 4.3:

$$\bar{u}_\mathrm{min} \approx \frac{\sigma_{\bar{u}}}{\sqrt{N_\mathrm{I}}}. \tag{29}$$

The maximum resolvable velocity is dependent upon the maximum particle displacement that can be afforded with a particle tracking algorithm:

$$u_\mathrm{max} = \frac{\Delta x_\mathrm{max}}{\Delta t}. \tag{30}$$

Accordingly, the dynamic velocity range for time-averaged measurements, $\overline{\mathrm{DVR}}$, obtained by the CVV equals

$$\overline{\mathrm{DVR}} = \sqrt{N_\mathrm{I}} \left(\frac{\Delta x_\mathrm{max}}{\sigma_{\bar{u}} \Delta t} \right). \tag{31}$$

For a CVV measurement where $u_\mathrm{max} \approx u_\infty$ and the turbulence intensity is 10%, this yields $\overline{\mathrm{DVR}} = 100$ when considering ensemble averaging bins with $N_\mathrm{I} = 100$. The ensemble averaging procedure allows for a larger $\overline{\mathrm{DVR}}$ than what would

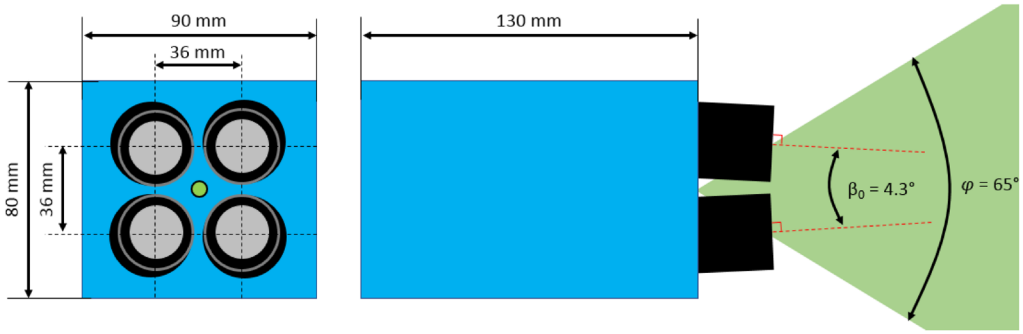

Figure 8. Sketch of the front (left) and side (right) of the CVV.

be possible using standard tomographic PIV (on the order of 30, Lynch and Scarano 2015).

The most common way to increase the $\overline{\text{DSR}}$ and $\overline{\text{DVR}}$ of the CVV is by collecting larger sequences of images, at detriment of the computation time.

6. Wind tunnel experiments

6.1. Prototype CVV system

A CVV system is realized that combines four cameras and laser illumination within a box as depicted in figure 8. Four compact LaVision *MiniShaker S* CMOS imagers (831 × 631 pixels at 471 fps, 10 bits) are positioned as schematically illustrated in figure 8. The cameras optical axes intersect at a point located at $z_0 = 50$ cm from the sensor plane with a corresponding base angle $\beta_0 = 4.3°$. The cameras are fitted with $f = 4$ mm lenses, with numerical aperture set to $f_\# = 8$ ensuring in-focus particle images over the expected volume depth ($z_{\max} \sim 0.5$ m). The light source is a Quantronix *Darwin-Duo* Nd-YLF laser (2 × 25 mJ pulse energy at 1 kHz). The light is transmitted from the source to the CVV through an optical fiber with its end in between the cameras (figure 8). The laser light spreading angle of 65° is achieved by focusing the collimated laser light at the source with a spherical lens of 20 mm focal length. An additional micro-lens is installed at the end of the optical fiber to further increase the spreading angle.

As previously discussed, given its working principle, the CVV system is unsuited for volumetric measurements with standard micron sized tracer particles, as these would not scatter sufficient light. Therefore HFSB (Bosbach *et al* 2009) with a diameter in the order of 300 μm are used as tracer particles.

The CVV is calibrated first by fitting a pinhole model to multiple recordings of a calibration plate (LaVision 'Type 30') and subsequently refined using volume self-calibration (Wieneke 2008). The CVV was found to be sufficiently rigid to allow for use of a single calibration at the beginning of each experimental campaign, also after movement of the CVV to a new measurement position.

6.2. Flow around a sphere

Experiments are performed in an open-jet low-speed wind tunnel with 60 × 60 cm^2 exit cross section at flow speed of 2.5 m s^{-1}. A sphere with a 10 cm diameter is placed 30 cm

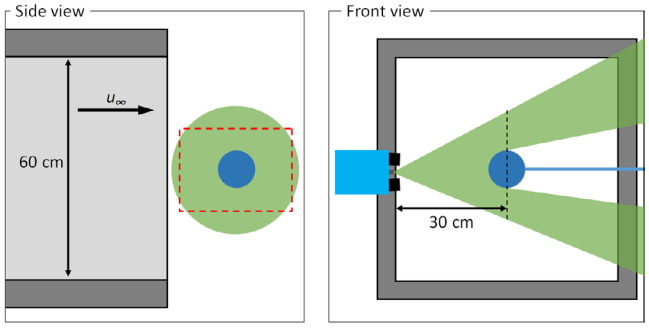

Figure 9. Schematic of the measurement setup. The figures are drawn in a plane through the center of the sphere.

downstream of the exit (figure 9). The Reynolds number based on the sphere diameter equals Re = $1.7 \cdot 10^4$. The CVV system is positioned just outside of the jet-stream at 30 cm distance from the sphere. The optical magnification at the center of the sphere is approximately 0.01.

The expected measurement volume width and height at this distance are 30 cm and 22 cm, respectively (indicated by the dashed red line in figure 9-left). The measurement volume encompasses the inviscid laminar flow region ahead of the sphere, and a turbulent wake, including a separated flow region behind the sphere. Such measurement with planar or tomographic PIV requires at least two measurement directions due to the model shadow and optical blockage to the cameras.

Particle images are recorded at 471 Hz, corresponding to a 5 mm displacement in the free stream (corresponding to approximately 15 pixels particle image displacement at $z = 30$ cm). Measurements include 15 runs, totaling 25 000 image quadruplets. The particle image density is limited by HFSB seeding generation rate and equals approximately $N_p = 0.015$ ppp. The instantaneous particle images from the four CVV cameras are shown in figure 10.

The figure shows the raw images for cameras 1, 2 and 3. Due to the small solid-angle of the imaging system, the differences between the four camera images is barely noticed by visual inspection. The time-series of images is pre-processed using a high-pass filter in the frequency domain (Butterworth filter, Sciacchitano and Scarano 2014) to reduce the reflections from the solid surface of the sphere (filter length of 7 recordings). The bottom-right figure shows the instantaneous particle image obtained by camera 4 after pre-processing. The particles peak intensity varies largely along the depth of the measurement volume (equation (5)) and decays moving away

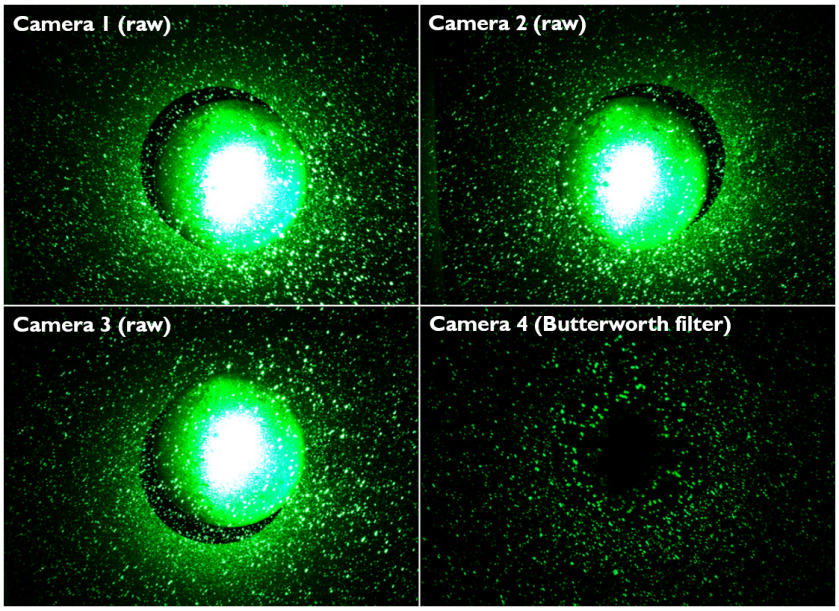

Figure 10. Raw instantaneous particle images from cameras 1–3 and the pre-processed particle image from camera 4 (bottom-right).

from the viewing axis due to the Gaussian profile of laser light intensity. The measurement volume achieved is approximately 10 liters, based on $z_{\min} = 15\,\text{cm}$ and $z_{\max} = 35\,\text{cm}$.

The center of the image is saturated where the light scattered by the surface of the sphere is reflected directly towards the imagers. As a result, no particle images can be detected in this region. Note that in the coaxial configuration, the illumination direction cannot be changed independently of the imagers viewing direction to reduce reflections. The effect of reflections can therefore not be reduced by changing illumination direction. Reflections could be reduced by use of paint or cameras with a larger full-well capacity. Alternatively, Jux *et al* (2018) show how the CVV measurement results from multiple viewing directions can be stitched together, providing an alternative strategy to mitigate surface reflections.

The sequence of pre-processed images is analyzed using the algorithm Shake-the-Box (STB, Schanz *et al* 2016) to estimate the particles velocity. Only tracks with a minimum length of 4-exposures are retained in the analysis. A 2nd order polynomial fit is used to regularize the particle trajectories, where a sliding track-fit through at most seven exposures is used. Approximately 0.1 tracks cm^{-3} are detected on average in every recording, which is less than the seeding concentration of 0.7 HFSB cm^{-3} estimated from the particle image density and equation (8).

For illustration, figure 11 shows a subset of tracked particles, colored by velocity magnitude. Particles at a distance larger than the sphere center plane are hidden for clarity of the visualization. The flow deceleration ahead of the stagnation point in front of the sphere is followed by a region where the flow accelerates beyond the free-stream value around the sphere under the effect of the favorable pressure gradient. After the point of maximum cross section, the boundary layer separates generating a turbulent wake region downstream of the sphere. In the latter, erratic particle trajectories can be observed, corresponding to the chaotic motions in the turbulent separated flow regime.

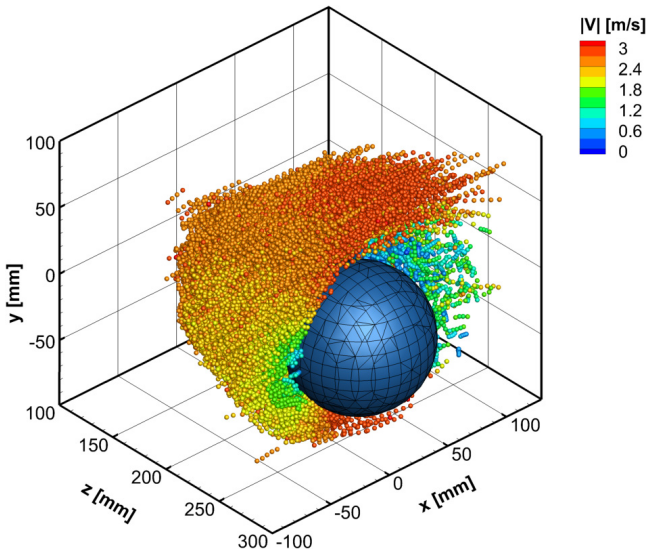

Figure 11. Subset of the particle tracks. The volume is cropped for clarity of the visualization.

The time-averaged velocity field is obtained by ensemble averaging the scattered data over bins of $7.5 \times 7.5 \times 7.5\,\text{mm}^3$. The evaluation with 75% overlap results in vectors spaced by 1.9 mm. The dynamic spatial range for this measurement is estimated to $\overline{\text{DSR}} = 25$. On average, there are $N_\text{I} = 500$ particles falling in every bin. Based on 10% intensity of the turbulent velocity fluctuations (wake region), the resulting $\overline{\text{DVR}}$ is in the order of 200.

The measured flow upstream of the sphere can be compared to the analytical solution from potential flow theory (e.g. Anderson (2010)). The measured time-averaged flow field is shown in figure 12-left (color contours), along with the velocity from potential flow theory (dashed contour lines). A generally good correspondence is observed within the angular range from the front stagnation point and moving approximately 45° along the surface of the sphere. Further than that

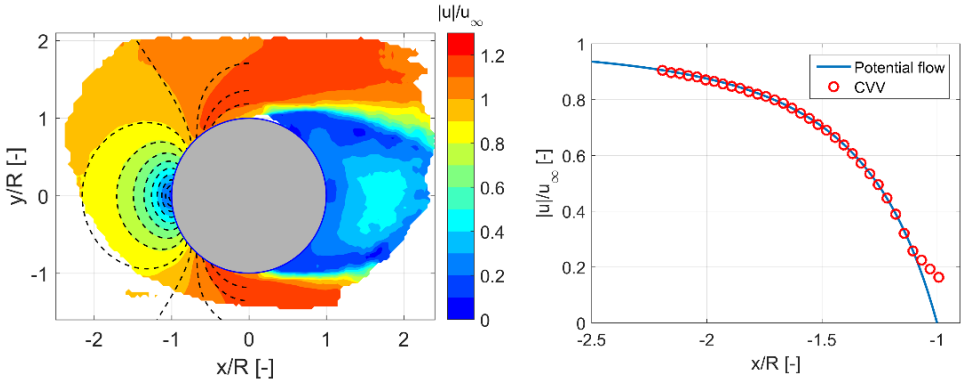

Figure 12. Left: Time-averaged velocity measurements of the flow around a sphere. Potential flow solution (dashed contours) superimposed on the CVV result. Right: Streamwise profile of velocity along the stagnation streamline.

point, the velocity field is affected by the separation in the rear of the sphere and the potential theory fails to adequately model the flow field. A detailed comparison is extracted along the stagnation streamline, where the velocity profile taken along $y = 0$ is considered (figure 12-right). The measured values correspond with good agreement to the theoretical reference up to $x/R = -1.1$. Any closer, the effect of the bin overlapping with the sphere yields an overestimation of velocity, similarly to the reported case of estimating the near wall velocity in boundary layers (Kähler *et al* 2012b).

The level of velocity fluctuations measured by the CVV away from the sphere gives an indication of the uncertainty of instantaneous velocity measurements. For the streamwise component $u'_{\mathrm{rms}} = 0.02$ m s^{-1} (approx. 1%), whereas along the depth $w'_{\mathrm{rms}} = 0.2$ m s^{-1} (approx. 8%). These values are obtained considering trajectories evaluated along 7-frames with a 2nd order polynomial. From a parametric analysis, the value of u'_{rms} is found to be independent of the chosen track length and is therefore considered to correspond to the physical velocity fluctuations exhibited by the free stream of the open jet. The value for w'_{rms} is significantly higher and in fair correspondence to the measurement error of the axial component predicted in section 4.2. Considering that the time-averaged value is built in each bin with an ensemble of approximately 500 samples, the uncertainty of the mean value becomes 0.05% for the streamwise component and 0.4% for w.

6.3. Full-scale cyclist measurements

Following the work on the relatively simple model of a sphere in the previous section, in the present section the CVV is used to measure the near-surface flow around a full-scale cyclist.

6.3.1. Experimental apparatus and setup. A full-scale 3d-printed model of *Giro d'Italia* winning cyclist Tom Dumoulin (van Tubergen *et al* 2017) is used for the present wind tunnel measurements. The measurements on the cyclist model were performed by Jux *et al* (2018) in an open jet wind tunnel facility with a 2.85 × 2.85 m^3 cross-section of the outlet. The wind tunnel speed of $u_\infty = 14$ m s^{-1} (Re $= 5.5 \cdot 10^5$) corresponds to that practiced during time-trial competitions (see e.g. the review by Lukes *et al* (2005)). A photograph of the experimental setup (figure 13) shows the cyclist inside of the test section, downstream of the HFSB seeding rake. The relatively compact size of the CVV makes it suitable for manipulation by a robot arm, as also shown in figure 13. A full discussion of the robotic manipulation of the CVV for measurement of an extended measurement volume is given in Jux *et al* (2018).

The present work considers three specific CVV measurements to illustrate the range of optical access, the data yield and the different types of utilization. The regions inspected (athlete's face, lower back and ankle-foot) are shown in figure 14-left. At the athlete's face, the measurement challenge lies in capturing the flow over a 3D corrugated surface. At the back of the athlete, the flow is expected to exhibit unsteady separation with high levels of turbulence. Finally, the ankle-foot region is known to be the source of tip vortices emanating from this extremity. Capturing these vortices gives an indication of the small scale velocity and vorticity scales that can be represented with the CVV.

The dashed red lines in figure 14-left show the approximate field of view employed for the measurements. The active area of the CVV imagers is cropped to 640 × 475 pixels to achieve a recording rate of 758 Hz that limits the particle image displacement within 18 mm (40 px at $z = 30$ cm) at a free-stream velocity of 14 m s^{-1}. From equation (1), a measurement volume width of 23 cm is expected at $z = 30$ cm. Reducing the conical expansion angle yields an increased measurement volume depth of approximately 70 cm. Based upon analysis of the aerodynamic interference of the robotic CVV in Jux *et al* (2018), z_{min} is taken at 20 cm. Each sequence includes 5000 recordings.

Samples of particle image recordings are shown in figure 14-right. The average particle image density is approximately $N_{\mathrm{p}} = 0.01$ ppp. Using image pre-processing and particle motion analysis procedures like in the previous section, one tenth of the particles are tracked successfully. The bin size for ensemble averaging is set to 20 × 20 × 20 mm^3 with 75% overlap (5 mm vector spacing). The criterion is imposed that a minimum of 10 velocity measurements are used to estimate the time-average value in each bin. Approximately 10% of the bins contain between 10 and 20 particles. On average

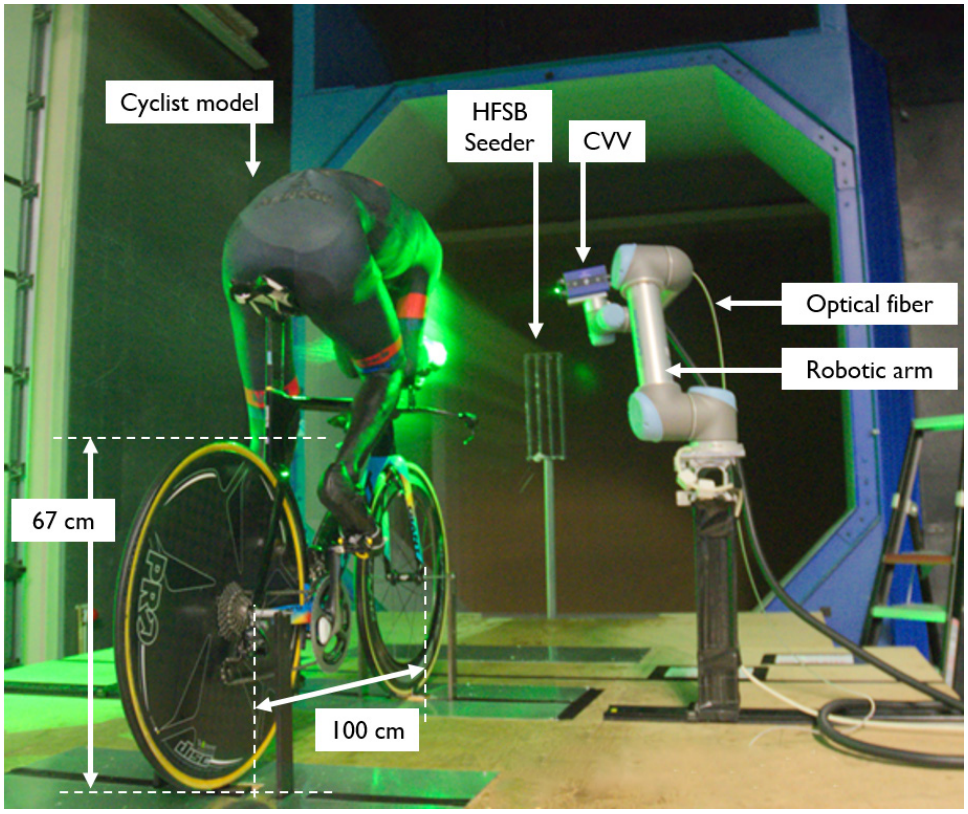

Figure 13. Photograph of the robotic CVV setup. Reproduced from Jux *et al* (2018). CC BY 4.0.

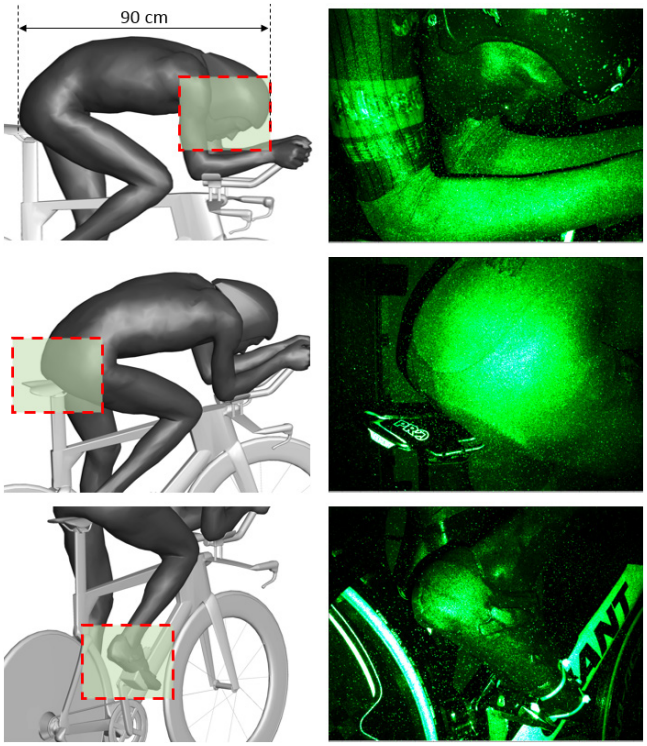

Figure 14. Field of view relative to the cyclist model indicated by the dashed red box (left) and example of a corresponding raw particle image (right). For clarity the particle images are colored green and saturated at 512 counts. From top to bottom the 'face', 'back' and 'foot' measurement cases are shown.

each bin contains on the order of 100 particles. Based on the volume depth of $z_{\min} - z_{\max} = 50\,\text{cm}$, the $\overline{\text{DSR}}$ is estimated to 25. Assuming a turbulence intensity of 10% and taking the average number of particles per bin yields $\overline{\text{DVR}} = 100$.

6.3.2. Near-surface streamlines. The flow near the face and arms of the cyclist exhibits stagnation on the biceps of right arm, which is positioned approximately perpendicular to the free-stream direction. The near-surface streamlines are computed from the CVV results at a distance of 5 mm (one vector-spacing) from the surface of the cyclist. The result is illustrated in figure 15, along with color contours of velocity magnitude distributed on the same surface.

The near surface streamlines on the forearm slightly diverge approaching the elbow, where a dividing stagnation line (red line) can be identified that starts on the side of the arm and curls up on top of the arm to continue over the top of the biceps. There is no indication of flow separation at the elbow as the direction of the velocity along the streamlines does not reverse. The separating streamline ends in a saddle point, where a secondary dividing stagnation line can be identified (dashed blue line) that goes through the saddle point.

The measurement domain also includes parts of the flow over the face of the cyclist. Here the more elaborate surface topology is accompanied by a more complex flow pattern. In general, the concave regions exhibit a lower velocity and the convex (protruding) regions see a local increase of the velocity. Inspection of the streamlines plotted near the face of the cyclist shows a dividing streamline on the cyclist's cheek.

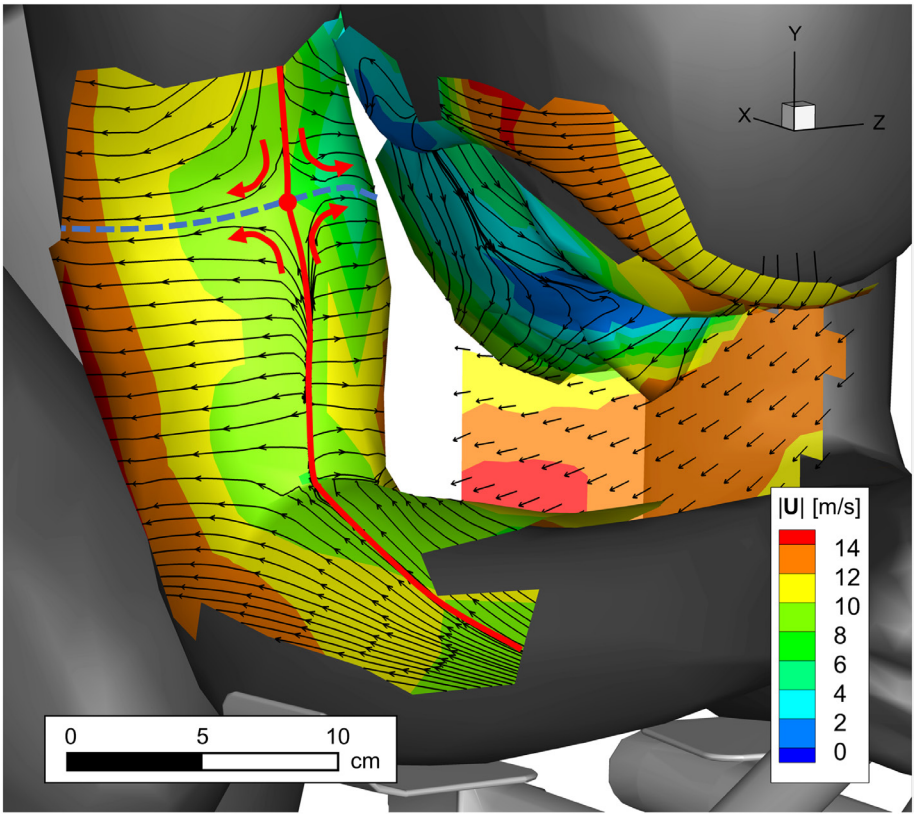

Figure 15. Streamlines in the face and arm region evaluated at 5 mm from the body of the cyclist, plotted on color contours of velocity magnitude; the scale indicates the size of the measurement volume. The results come from a single CVV measurement location. Velocity vectors are sub-sampled by a factor 3.

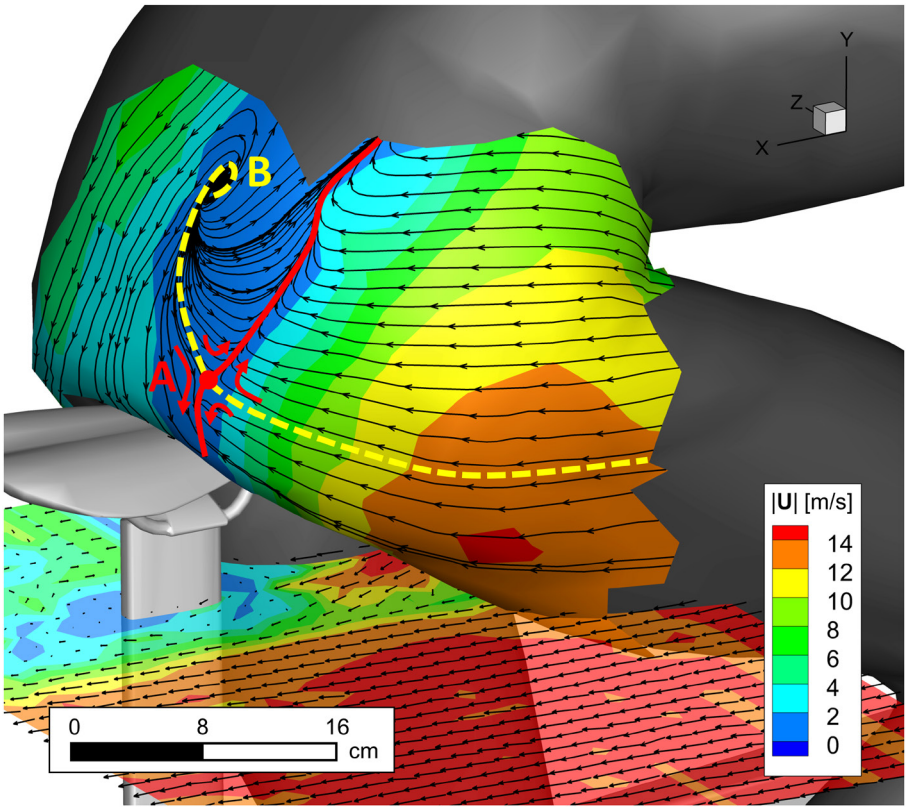

Figure 16. Streamlines in the back region evaluated at 5 mm from the body of the cyclist, plotted on color contours of velocity magnitude; the scale indicates the size of the measurement volume. The results come from a single CVV measurement location. Velocity vectors sub-sampled by a factor 3.

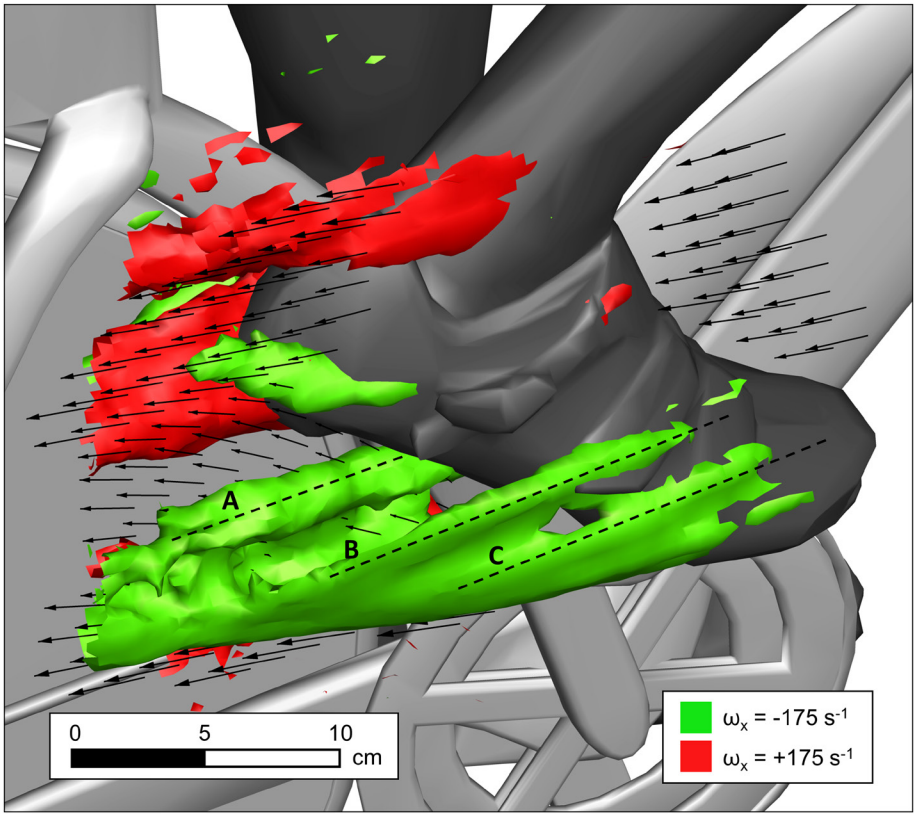

Figure 17. Isosurface visualization of streamwise vorticity. An approximate scaling is included to indicate the size of the measurement volume. The results come from a single CVV measurement location. Velocity vectors sub-sampled by a factor 3.

Above this streamline, near the eye of the cyclist, a region of reverse flow is observed. A slice of the velocity field plotted in the region between the face and the arms indicates the flow underneath the face accelerates as a result of the reduced cross section available.

Moving to the back of the cyclist (second field of view in figure 14), flow separation is expected on the relatively flat shaped lower back of the athlete. In figure 16 the near-surface streamlines confirm the above.

The flow pattern is however not as intuitive, as a dividing separation line (red line) appears at an asymmetric position and runs downward along the cyclist back where it crosses at a saddle point and another separating streamline that is spiraling upward and ending up at approximately the Ilium. The spiraling pattern of this surface streamline suggests that the shear layer separating around this region is wrapped up into a tornado like vortex, rapidly tilting and developing along the stream-wise direction. This observation confirms the 3D flow topology hypothesized in the study of Crouch *et al* (2014).

The color contoured velocity magnitude indicates that the separated flow region is fairly limited to a fraction of the low-back region, with the caveat, however, that the velocity is sampled here at approximately 5 mm distance from the solid surface. A slice of the velocity field downstream of the right upper leg indicates that the flow rapidly recovers the free-stream conditions after only a fraction of the leg cross-section diameter.

6.3.3. Ankle-foot vortices. The field of view containing the right shoe of the cyclist (figure 14-bottom) is considered to visualize the vortical structures developing around in the shoe and ankle region. The green and red isosurfaces in figure 17 represent negative and positive streamwise vorticity, respectively. Elongated vortices (*A*, *B* and *C*) emanate from the sides of the shoe.

Vortices from each side have the same direction of rotation and merge into a single structure. A counter-rotating vortex (red) originates from the ankle and heel regions. The distance between the vortices *B* and *C* is approximately 30 mm, which is close to the spatial resolution limit of the current measurements, based on a bin size of 20 mm. Evaluating *a posteriori* the $\overline{\mathrm{DSR}}$ based on this length scale and the measurement volume depth of 500 mm yields approximately $\overline{\mathrm{DSR}} = 17$.

7. Conclusions

A coaxial volumetric velocimeter (CVV) is proposed based on the use of multiple imagers positioned close together and at a small solid angle. Illumination of tracer particles is provided through an optical fiber positioned in between the cameras. The CVV therefore requires optical access only from one measurement direction. In this configuration, the particle image intensity recorded on the imagers scatters with the 4th power of the particle distance from the measurement device.

The theoretical background derived in the study shows that the CVV is only of practical use when tracer particles are used that scatter light several orders of magnitude more than traditional fog droplets. Presently, the use of CVV is demonstrated making use of HFSB as tracers. In addition, the study shows that due to the small solid angle of the system there is an approximately 15-fold higher particle positional and velocity measurement error for the axial component than for the in-plane components. To compensate for reduced accuracy of the z-component of velocity, particles are imaged multiple times along their trajectories to produce a time-accurate reconstruction of their motion. The spatial resolution of the time-averaged velocity measurements depends upon the particle image density and the number of recordings. A spatial resolution of less than a centimeter is achieved currently only when employing an ensemble averaging approach over several thousand images.

A prototype CVV system has been employed for two wind tunnel experiments. The measured flow ahead of a sphere returns very good agreement with the potential flow theory.

Measurements in three regions around a full-scale cyclist model show the capability of the CVV to access the near-wall velocity over a complex 3D topology. Streamlines near the surfaces can be inferred as an approximation of skin-friction lines, yielding the details of near-wall flow topology. The time-average vorticity field also illustrates the potential to represent the vortex skeleton developing around a complex 3D body. The current levels of dynamic spatial and velocity range ($\overline{\text{DSR}}$ ~ 10, $\overline{\text{DVR}}$ ~ 100) lie below those typically achieved with planar PIV measurements. Both $\overline{\text{DSR}}$ and $\overline{\text{DVR}}$ depend upon the amount of tracers collected in the measurement bin. Therefore, experiments at higher resolution and accuracy require collecting larger data sets.

Acknowledgments

The contribution of Bernd Wieneke acknowledged for fruitful discussions on the CVV design. This research is supported by LaVision GmbH.

ORCID iDs

Jan F G Schneiders https://orcid.org/0000-0001-9506-3650

References

Adrian R J 1991 Particle-imaging techniques for experimental fluid mechanics *Annu. Rev. Fluid Mech.* **23** 261–304
Adrian R J 1997 Dynamic ranges of velocity and spatial resolution of particle image velocimetry *Meas. Sci. Technol.* **8** 1393
Adrian R J and Westerweel J 2011 *Particle Image Velocimetry* (Cambridge: Cambridge University Press)
Agüera N, Cafiero G, Astarita T and Discetti S 2016 Ensemble 3D PTV for high resolution turbulent statistics *Meas. Sci. Technol.* **27** 124011
Anderson J D 2010 *Fundamentals of Aerodynamics* (New York: McGraw-Hill)
Boillot A and Prasad A K 1996 Optimization procedure for pulse separation in cross-correlation PIV *Exp. Fluids* **21** 87–93
Bosbach J, Kühn M and Wagner C 2009 Large scale particle image velocimetry with helium filled soap bubbles *Exp. Fluids* **46** 539–47
Caridi G C A and Sciacchitano A 2017 Light scattering behaviour of Helium filled soap bubbles *Proc. 12th Int. Symp. Particle Image Velocimetry (Busan, Republic of Korea)*
Caridi G C A, Ragni D, Sciacchitano A and Scarano F 2016 HFSB-seeding for large-scale tomographic PIV in wind tunnels *Exp. Fluids* **57** 190
Cierpka C, Lütke B and Kähler C J 2013 Higher order multi-frame particle tracking velocimetry *Exp. Fluids* **54** 1533
Crouch T N, Burton D, Brown N A T, Thompson M C and Sheridan J 2014 Flow topology in the wake of a cyclist and its effect on aerodynamic drag *J. Fluid Mech.* **748** 5–35
Depardon S, Lasserre J J, Boueilh J C, Brizzi L E and Borée J 2005 Skin friction pattern analysis using near-wall PIV *Exp. Fluids* **39** 805–18
Durst F, Melling A and Whitelaw J H 1976 Principles and practice of laser-Doppler anemometry *NASA STI/Recon Technical Report A* 76 47019
Elsinga G E, Scarano F, Wieneke B and van Oudheusden B W 2006 Tomographic particle image velocimetry *Exp. Fluids* **41** 933–47
Fahringer T W, Lynch K P and Thurow B S 2015 Volumetric particle image velocimetry with a single plenoptic camera *Meas. Sci. Technol.* **26** 115201
Gesemann S, Huhn F, Schanz D and Schröder A 2016 From noisy particle tracks to velocity, acceleration and pressure fields using B-splines and penalties *18th Int. Symp. Applications of Laser and Imaging Techniques to Fluid Mechanics (Lisbon, Portugal, 4–7 July)*
Hain R and Kähler C J 2006 Single camera volumetric velocity measurements using optical aberrations *12th Int. Symp. on Flow Visualization (Göttingen, Germany, 10–14 September)*
Jeon Y J, Chatellier L and David L 2014 Fluid trajectory evaluation based on an ensemble-averaged cross-correlation in time-resolved PIV *Exp. Fluids* **55** 1766
Johnson K C, Thurow B S, Blois G and Christensen K T 2017 Volumetric velocity measurements in the wake of a hemispherical roughness element *AIAA J.* **55** 2158–73
Jux C, Sciacchitano A, Schneiders J F G and Scarano F 2018 Robotic volumetric PIV of a full-scale cyclist *Exp. Fluids* **59** 74
Kähler C J, Scharnowski S and Cierpka C 2012a On the resolution limit of digital particle image velocimetry *Exp. Fluids* **52** 1629–39
Kähler C J, Scharnowski S and Cierpka C 2012b On the uncertainty of digital PIV and PTV near walls *Exp. Fluids* **52** 1641–56
Kähler C J, Scholz U and Ortmanns J 2006 Wall-shear-stress and near-wall turbulence measurements up to single pixel resolution by means of long distance micro-PIV *Exp. Fluids* **41** 327–41
Larmore L 1965 *Introduction to Photographic Principles* 2nd edn (New York: Dover)
Lukes R A, Chin S B and Haake S J 2005 The understanding and development of cycling aerodynamics *Sports Eng.* **8.2** 59–74
Lynch K P and Scarano F 2013 A high-order time-accurate interrogation method for time-resolved PIV *Meas. Sci. Technol.* **24** 035305
Meng H, Pan G, Pu Y and Woodward S H 2004 Holographic particle image velocimetry: from film to digital recording *Meas. Sci. Technol.* **15** 673
Novara M and Scarano F 2013 A particle-tracking approach for accurate material derivative measurements with tomographic PIV *Exp. Fluids* **54** 1584

Pothos S, Troolin D, Wing L and Ragan M 2009 V3V-volumetric three-component velocimetry for 3D flow measurements main principle, theory and applications *Revista Termotehnica* **2** 2009

Raffel M, Willert C and Kompenhans J 2007 *Particle Image Velocimetry: a Practical Guide* (Berlin: Springer) https://doi.org/10.1007/978-3-540-72308-0

Savitzky A and Golay M J E 1964 Smoothing and differentiation of data by simplified least squares procedures *Anal. Chem.* **36** 1627–39

Scarano F 2013 Tomographic PIV: principles and practice *Meas. Sci. Technol.* **24** 012001

Scarano F, Ghaemi S, Caridi G C A, Bosbach J, Dierksheide U and Sciacchitano A 2015 On the use of helium-filled soap bubbles for large-scale tomographic PIV in wind tunnel experiments *Exp. Fluids* **56** 42

Schanz D, Gesemann S and Schröder A 2016 Shake the Box: Lagrangian particle tracking at high particle image densities *Exp. Fluids* **57** 70

Schanz D, Schröder A, Gesemann S, Michaelis D and Wieneke B 2013 Shake-the-Box: a highly efficient and accurate tomographic particle tracking velocimetry (TOMO-PTV) method using prediction of particle position *10th Int. Symp. on Particle Image Velocimetry—PIV13 (Delft, The Netherlands, 1–3 July 2013)*

Schneiders J F G and Sciacchitano A 2017 Track benchmarking method for uncertainty quantification of particle tracking velocimetry interpolations *Meas. Sci. Technol.* **28** 065302

Schneiders J F G, Caridi G C A, Sciacchitano A and Scarano F 2016 Large-scale volumetric pressure from tomographic PTV with HFSB tracers *Exp. Fluids* **57** 164

Sciacchitano A and Scarano F 2014 Elimination of PIV light reflections via a temporal high pass filter *Meas. Sci. Technol.* **25** 084009

Talapatra S and Katz J 2012 Three-dimensional velocity measurements in a roughness sublayer using microscopic digital in-line holography and optical index matching *Meas. Sci. Technol.* **24** 024004

van Tubergen J, Verlinden J, Stroober M and Baldewsing R 2017 Suited for performance: fast full-scale replication of athlete with FDM *Proc. 1st Annual ACM Symp. on Computational Fabrication (Cambridge, Massachusetts, 12–13 June)*

Wieneke B 2008 Volume self-calibration for 3D particle image velocimetry *Exp. Fluids* **45** 549–56

Willert C E and Gharib M 1992 Three-dimensional particle imaging with a single camera *Exp. Fluids* **12** 353–8